45th AIAA Aerospace Sciences Meeting and Exhibit
8 - 11 January 2007, Reno, Nevada

AIAA 2007-826

Towards Predicting Supersonic, Hot Jet Noise

Xiaodan Cai*, Foluso Ladeinde†, Kehinde Alabi‡
Thaerocomp Technical Corporation, P.O. Box 1527, Stony Brook, NY 11790

The noise from supersonic jet aircraft during landing and taking-off poses serious environmental challenge to military bases. Two RANS-based acoustic source models have been used to calculate the noise signature from a supersonic, hot jet flow, one is based on the MGBK method from Khavaran et al. [12] and the other one is from Tam and Auriault [13]. The aerodynamic predictions from our RANS calculation with high-order numerical schemes and modified *k-ε* models agree well with experimental data. However, it is found that both acoustic models have only limited success in predicting the far-field sound spectrum especially for shallow aft-angles, while the MGBK method has a slightly better performance over Tam's method for the prediction of overall sound pressure levels. The large-eddy simulation approach is suggested to use for predicting supersonic, hot jet noise.

Nomenclature

$\hat{U}$ = conservative flow variables
$\hat{F}$ = inviscid flux terms in the ξ-direction
$\hat{G}$ = inviscid flux terms in the η-direction
$\hat{H}$ = inviscid flux terms in the ζ-direction
$\hat{F}_v$ = viscous flux terms in the ξ-direction
$\hat{G}_v$ = viscous flux terms in the η-direction
$\hat{H}_v$ = viscous flux terms in the ζ-direction
J = metrics Jacobian
U^P = conservative flow variables in the p-th sub-iteration step
Δt = global time step
Δt_s = sub-iteration time step
$\tilde{R}_{Roe}$ = right eigen-vectors of Roe-averaged flux matrices
Re = Reynolds number
M_∞ = free-stream Mach number
M_j = jet-exit Mach number
k = turbulent kinetic energy
ε = turbulent kinetic energy dissipation rate
δ_ξ = finite-difference in the ξ-direction
$S(\vec{x},\omega)$ = the noise spectrum with frequency ω at observation point $\vec{x}$
$\langle p^2(\vec{x},\omega)\rangle$ = the noise spectrum with frequency ω at observation point $\vec{x}$

*Senior Research Engineer, AIAA Member.
†Associate Fellow, AIAA.
‡Research Engineer, AIAA Member.

$p^a(\vec{x}_1, \vec{x}, \omega)$ = adjoint green function with sound source at $\vec{x}_1$ to the observation point $\vec{x}$

I. Introduction

The supersonic engine jet noise on taking-off and landing approach of a JSF (Joint-Striker-Fighter) is a serious environmental concern to military bases. Modeling of the noise characteristics of aircraft gas turbine engines is much needed to facilitate early evaluation of environmental impact and to enable analysis of technology and methods to control noise.

However, predicting supersonic jet noise is not an easy task. First, the noise generating mechanism in supersonic is very complex [1]. Except for jets operating at perfectly expanded conditions, the supersonic jet noise comprises three major components: the turbulent mixing noise, the broadband shock-associated noise and the screech tones. The relative intensity of the three noise components is a strong function of the nozzle operation conditions and the direction of observation. In the downstream direction of the jet, turbulent mixing noise is usually the most dominant noise component. And in the upstream direction, the broadband shock-associated noise is more intense. Moreover, the supersonic jet noises are also affected significantly by the forward flight effects and the temperature effects [2]. In this paper, we will focus on the prediction methods addressing the temperature effects and forward flight effects on the mixing noise.

Traditionally, the prediction model of jet mixing noise was based on the acoustic analogy developed by Lighthill [3, 4], who rearranged the full equations of motion in the form of a linear wave equation, with equivalent acoustic sources that depend on the mean and turbulent fields. At low Mach number flow, Lighthill was able to use the similarity laws of high-Reynolds number turbulent jets to predict that the overall mean square pressure radiated from a jet should scale as the eighth power of the jet velocity in a simple jet flow. Since then, knowledge of the scaling laws together with detailed measurements on datum jets has allowed accurate predictions of the radiated noise from other similar jets to be made without the need for a detailed knowledge of the equivalent acoustic sources. For single jets, this has led to several semi-empirical prediction schemes such as that based on the ESDU database [5], while for coaxial jets, an extension of this methodology has been proposed by Fisher et al. [6,7] in their Four Source Model.

However, for modern engine with complex nozzle geometries specifically designed to alter the turbulent properties of the flow for acoustic benefits, simple scaling laws are unlikely to hold and the traditional semi-empirical prediction schemes will be ineffective without a large (and impractical) amount of data being collected. Moreover, in any case, a purely empirical scheme of this type offers no insight to the nozzle designer who wishes to reduce jet noise levels. To move forward, it is necessary to measure, or model in a rational manner, both the mean and turbulent properties of the flow so that a realistic estimate of the equivalent acoustic sources can be made, as well as the influence of the mean flow on the propagation of the resulting acoustic waves through and out of the jet.

In principle the entire jet noise prediction could be accomplished by a full unsteady CFD/CAA calculation, but the complexities associated with such a task for high Reynolds number jet flows mean that this is unlikely to be practical for many years to come. One possible resolution of these difficulties is to use a relatively fast-running CFD code, such as a Reynolds-averaged Navier–Stokes (RANS) scheme, to generate input data for acoustic source and propagation models.

Coupling an acoustic source model to a steady flow prediction is not new and was considered as long ago as 1977 by Balsa and Gliebe [8] and Mani et al. [9]. Their scheme is generally referred to as the MGB method and has been extended by Khavaran [10-12] to use a RANS solution based on a k– ε turbulence model (the MGBK method). Recently Tam and Auriault [13] have also used a k–ε turbulence model with a RANS solver to provide the inputs for the acoustic source model; the subsequent propagation of sound was described by solving the linearized Euler equations. The resulting predictions are claimed to be in good agreement with measured data. However, while the MGB, the MGBK, and similar approaches all either use Lighthill's acoustic analogy, or variants such as the Lilley [14] formulation of the acoustic analogy, Tam and Auriault use an apparently novel source model which they develop in analogy to the kinetic theory of gases. In this paper, we will compare and evaluate the performance of Tam's and Khavaran's models in predicting supersonic jet mixing noises.

Moreover, a high-fidelity CFD method [15] for accurate, affordable, efficient and reliable flow calculations, which is essential in this case, have been introduced and applied to supersonic jet flow calculations with complex nozzle geometries. The unique features of our high-fidelity CFD method include: high accuracy order numerical schemes for all-speed calculations (6-th order compact scheme is used for subsonic flows and 5-th order WENO scheme for shock-embedded flows); high-order overset procedure for multi-block calculations with complex geometries. The benefits and pitfalls of using our high-order CFD scheme for practical engineering problems have been identified and demonstrated in our previous work [15-16]. The following section briefly describes our numerical procedures.

II. Governing Equations

2.1 Flow Solver

The numerical scheme used to calculate the flow is based on high-order procedures for both subsonic and supersonic flows, and is consistent with the flow of equations being written as:

$$\frac{\partial \hat{U}}{\partial t}+\frac{\partial}{\partial \xi}\left(\hat{F}-\frac{1}{\mathrm{Re}}\hat{F}_v\right)+\frac{\partial}{\partial \eta}\left(\hat{G}-\frac{1}{\mathrm{Re}}\hat{G}_v\right)+\frac{\partial}{\partial \zeta}\left(\hat{H}-\frac{1}{\mathrm{Re}}\hat{H}_v\right)=0, \tag{1}$$

where $\hat{U}=1/J\cdot\left(\rho,\rho u,\rho v,\rho w,\rho E\right)^T$, and $\hat{F},\hat{G},\hat{H}$ are inviscid flux terms, $\hat{F}_v,\hat{G}_v,\hat{H}_v$ are the viscous flux terms ([15]). By using the implicit approximately-factored finite-difference algorithm of Beam-Warming and employing a Newton-like sub-iteration, the following numerical algorithm results:

$$\begin{aligned}
&\left[\left(J^{-1}\right)^{p+1}+\phi^i\Delta t_s\delta_\xi\left(\frac{\partial \hat{F}^{\,p}}{\partial U}-\frac{1}{\mathrm{Re}}\frac{\partial \hat{F}_v{}^{p}}{\partial U}\right)\right]J^{p+1}\times\left[\left(J^{-1}\right)^{p+1}+\phi^i\Delta t_s\delta_\eta\left(\frac{\partial \hat{G}^{\,p}}{\partial U}-\frac{1}{\mathrm{Re}}\frac{\partial \hat{G}_v{}^{p}}{\partial U}\right)\right]J^{p+1}\times\\
&\qquad\left[\left(J^{-1}\right)^{p+1}+\phi^i\Delta t_s\delta_\zeta\left(\frac{\partial \hat{H}^{\,p}}{\partial U}-\frac{1}{\mathrm{Re}}\frac{\partial \hat{H}_v{}^{p}}{\partial U}\right)\right]\cdot\Delta U\\
&=-\phi^i\Delta t_s\left[\left(J^{-1}\right)^{p+1}\frac{(1+\phi)U^p-(1+2\phi)U^n+\phi U^{n-1}}{\Delta t}-U^p\left(\left(\frac{\xi_t}{J}\right)_\xi+\left(\frac{\eta_t}{J}\right)_\eta+\left(\frac{\varsigma_t}{J}\right)_\varsigma\right)\right]\\
&-\phi^i\Delta t_s\left[\delta_\xi\left(\hat{F}^{\,p}-\frac{1}{\mathrm{Re}}\hat{F}_v{}^{p}\right)+\delta_\eta\left(\hat{G}^{\,p}-\frac{1}{\mathrm{Re}}\hat{G}_v{}^{p}\right)+\delta_\zeta\left(\hat{H}^{\,p}-\frac{1}{\mathrm{Re}}\hat{H}_v{}^{p}\right)\right],
\end{aligned} \tag{2}$$

where

$$\phi^i=\frac{1}{1+\phi},\Delta U=U^{p+1}-U^p.$$

Either a first or second-order temporal accuracy can be specified in the above iterative procedure by selecting $\phi=0$ or $\phi=1/2$, and p is the sub-iteration index. For $p=1$, $U^p=U^n$ and as $p\to\infty$, $U^p\to U^{n+1}$. In the above expression, the geometric conservation law (GCL)

$$\frac{\partial J^{-1}}{\partial t}+\left(\frac{\xi_t}{J}\right)_\xi+\left(\frac{\eta_t}{J}\right)_\eta+\left(\frac{\zeta_t}{J}\right)_\zeta=0 \tag{3}$$

has been used to evaluate the term $\dfrac{\partial J^{-1}}{\partial t}$, which ensures satisfaction of the GCL for moving meshes.

The spatial discretization procedure used in our work is one of the few to implement the WENO scheme [15] in a curvilinear coordinate system. The use of the high-order shock-capturing method is very beneficial to supersonic jet flow calculations: The characteristic-wise WENO-LLF scheme is used to evaluate the inviscid flux-terms. For example, its formula for the flux-term in ξ-direction in curvilinear coordinate system can be written as:

$$\delta_\xi\hat{F}=\frac{1}{\Delta\xi}\left\{\left[\widetilde{\mathbf{R}}_{Roe}\cdot\left(\widetilde{\mathbf{R}}_{Roe}^{-1}\cdot\hat{F}\right)\right]_{i+1/2}-\left[\widetilde{\mathbf{R}}_{Roe}\cdot\left(\widetilde{\mathbf{R}}_{Roe}^{-1}\cdot\hat{F}\right)\right]_{i-1/2}\right\}=\frac{1}{\Delta\xi}\left\{\widetilde{\mathbf{R}}_{Roe,i+1/2}\cdot\mathbf{f}_{i+1/2}-\widetilde{\mathbf{R}}_{Roe,i-1/2}\cdot\mathbf{f}_{i-1/2}\right\}, \tag{4}$$

where the p-th characteristic component (**f**) is represented by

$$f_{i+1/2}^{(p)} = \hat{v}_{i+1/2,r}^{+} + \hat{v}_{i+1/2,r}^{-}. \tag{5}$$

The two functions $\hat{v}^{\pm}$ are defined by

$$\hat{v}^{\pm} = \frac{1}{2}\tilde{\mathbf{R}}_{Roe,i+1/2}^{-1}\left(\hat{F} \pm \alpha_{i+1/2}^{(p)}\hat{U}\right), \tag{6}$$

and the values of $\hat{v}_{i+1/2,r}^{\pm}$ are computed using the $(2r+1)$th-order WENO scheme as given by

$$\hat{v}_{i+1/2,r}^{\pm} = \sum_{s=s_{\min}^{\pm}}^{s_{\max}^{\pm}} \omega_{r,s}\left(\hat{v}^{\pm}\right) \sum_{j=0}^{r} a_{r,s,j}^{\pm} \hat{v}_{i-r+s+j}^{\pm}, \tag{7}$$

where the range of indices is bounded with $s_{\min}^{+} = 0,\ s_{\max}^{+} = r$ or with $s_{\min}^{-} = 1,\ s_{\max}^{-} = r+1$, and the values of coefficients $a_{r,s,j}^{\pm}$ and weights $\omega_{r,s}$ can be computed or obtained from Ref.[17].

To reduce free stream preservation errors, metric evaluation is treated by an averaging procedure similar to that of the Lax-Friedrichs approach for the dependent variables:

$$x_{i+1/2} = x_{i+1/2,r}^{+} + x_{i+1/2,r}^{-}, \tag{8}$$

where the values of $x_{i+1/2,r}^{\pm}$ are computed using a WENO stencil as in Eq. (7).

Our overset method is based on a high-order shock-capturing interpolation procedure ([18]). Instead of using a central-point stencil to interpolate the values at the overset node, our method uses a discontinuity-sensing procedure to determine the donor points, and then uses the following Lagrangian formulation to obtain the field values at the overset node points:

$$\phi = \sum_{k=0}^{m-1}\left(\prod_{\substack{i=0 \\ i\neq k}}^{m-1}(\delta - i)\right) R(k)\phi_k, \tag{9}$$

$$R(k) = \frac{-1^{m+k-1}}{(m-k-1)!k!},$$

where m is the pre-determined order of the interpolation and δ is the distance of the interpolated point from the left-most point of the stencil.

The modified $k-\varepsilon$ model is based on Tam's work ([19]), which considers the vortex-stretching effects ([20]) and the compressibility effects ([21]) and is written as

$$\frac{\partial k}{\partial t} + u_j\frac{\partial k}{\partial x_j} = \frac{\mathrm{Re}^{-1}}{\rho}\mu_t S_{ij}S_{ij} - \mathrm{Re}\cdot\varepsilon^{s} + \frac{\mathrm{Re}^{-1}}{\rho}\frac{\partial}{\partial x_j}\left(\left(\mu + \frac{\mu_t}{\sigma_k}\right)\frac{\partial k}{\partial x_j}\right), \tag{10}$$

$$\frac{\partial \varepsilon}{\partial t} + u_j\frac{\partial \varepsilon}{\partial x_j} = \frac{\mathrm{Re}^{-1}}{\rho}C_{\varepsilon 1}\frac{\varepsilon}{k}\mu_t S_{ij}S_{ij} - \mathrm{Re}\cdot(C_{\varepsilon 2}f_2 - C_{\varepsilon 3}\chi\cdot\mathrm{Re}^{-3})\frac{\varepsilon^2}{k} + \frac{\mathrm{Re}^{-1}}{\rho}\frac{\partial}{\partial x_j}\left(\left(\mu + \frac{\tilde{\mu}_t}{\sigma_\varepsilon}\right)\frac{\partial \varepsilon}{\partial x_j}\right) \tag{11}$$

where the turbulent kinetic energy and its dissipation rate are normalized as: $k = \frac{\tilde{k}}{\tilde{u}_\infty^2}$, and $\varepsilon = \frac{\tilde{\mu}_\infty\tilde{\varepsilon}}{\tilde{\rho}_\infty\tilde{u}_\infty^4}$. The newly-defined dissipation rate ε^{s} is represented by

$$\varepsilon^s = \varepsilon\left(1+\alpha M_t^2\right), \tag{12}$$

and the stretching effect term, χ, is defined as

$$\chi = \omega_{ij}\cdot\omega_{jl}\cdot s_{li}, \tag{13}$$

where $M_t^2 = \frac{2k}{T}M_j^2$, $\omega_{ij} = \frac{1}{2}\frac{k}{\varepsilon}\left(\frac{\partial u_i}{\partial x_j} - \frac{\partial u_j}{\partial x_i}\right)$ and $s_{li} = \frac{1}{2}\frac{k}{\varepsilon}\left(\frac{\partial u_i}{\partial x_l} + \frac{\partial u_l}{\partial x_i}\right)$.

The model constants are set as:

$$\begin{aligned} C_\mu &= 0.0874, \quad \alpha = 0.518, \\ C_{\varepsilon 1} &= 1.40, \quad C_{\varepsilon 2} = 2.02, \quad C_{\varepsilon 3} = 0.822, \\ \gamma\sigma_T &= \Pr = 0.422, \quad \sigma_k = 0.324, \quad \sigma_\varepsilon = 0.377 \end{aligned} \tag{14}$$

2.2 Acoustic Model

Both Tam's and Khavaran's acoustic models use a RANS solution as the inputs, and the RANS solution is obtained by a modified k– ε turbulence model (see previous report for its formulation). Here we give only the acoustic source models.

a) Method One (Tam's Model)

In Tam's model, the noise spectrum in the far field is given by

$$S(\vec{x},\omega) = \frac{4\pi^3}{\rho_\infty c_\infty (\ln 2)^{3/2}} \int_{JET} \left|p^a(\vec{x}_2,\vec{x},\omega)\right|^2 \frac{\Gamma\left(\nu+\frac{1}{2}\right)}{\Gamma(\nu)} \frac{\hat{q}_s^2}{c^2\tau_s} l_s^3 \frac{\exp\left\{-\frac{\omega^2 l_s^2}{4\bar{u}^2\ln 2}\right\}}{\left[1+\omega^2\tau_s^2(1-M_c\cos\theta)\right]^{\nu+1/2}} d\vec{x}_2 \tag{15}$$

where $p^a(\vec{x}_1,\vec{x},\omega)$ is the adjoint Green function with source point at $\vec{x}$ and observation point at $\vec{x}_1$, which is determined by the equation given in the followings. The three model parameters, l_s (the turbulent length scale), τ_s (the turbulent time scale) and $\hat{q}_s$ (a measure of the turbulent intensity), are given by ([13]):

$$l_s = c_l\left(\kappa^{1.5}/\varepsilon\right), \quad \tau_s = c_\tau(\kappa/\varepsilon), \quad \hat{q}_s^2/c^2 = A^2\left(\frac{2}{3}\kappa\right)^2, \tag{16}$$

where the model constants are calibrated with experimental data as ([13]):

$$c_l = 0.256, \quad c_\tau = 0.233, \quad A = 0.755. \tag{17}$$

b) Method Two (Khavaran's Model)

In Khavaran's acoustic model ([12]), the sound comprises of two components: the self noise and the shear noise. The self-sound spectrum per unit ring volume at radius r^s is given by:

$$\left\langle \overline{p_{self}^2}\left(\vec{x},\vec{x}^s,\omega\right)\right\rangle \cong \frac{1}{(4\pi R)^2}\frac{(1-M^s\cos(\theta))^6}{(1-M_c\cos(\theta))^2}\left(\frac{\rho^s}{\bar{p}_\infty}\right)^2 \left(\rho_\infty^2 I_{1111}\right)k^4 \sum_m \left|f_m\left(r^s,k,\theta\right)\right|^2$$

(4) (18)

and the shear-sound spectrum per unit ring volume at radius r^s is given by:

$$\left\langle \overline{p^2_{shear}}\left(\vec{x},\vec{x}^{\,s},\omega\right)\right\rangle \cong \frac{1}{(4\pi R)^2}\frac{\left(\dfrac{2dU/dr}{\omega}\right)^2}{(1-M_c\cos(\theta))^2}\left(\frac{7}{2}\cos^2\theta\right)^2\left(\cos^2\theta+\frac{\left(1-M^s\cos\theta\right)^2}{c^2/c_\infty^2}\right) \quad (19)$$
(5)
$$\bullet\left(\rho_\infty^2 I_{1111}\right)k^4\sum_m\left|f_m\left(r^s,k,\theta\right)\right|^2.$$

where $f_m\left(r^s,k,\theta\right)$ comes from the adjoint green functions of the linearized Lilley equation. In Eqs. (18) and (19), the 4th-order axial correlation, I_{1111} is modeled by

$$I_{1111}\left(\vec{x}^{\,s},\Omega\right)=A_m\kappa^{3.5}\tau_0^4\frac{K_1\left[\sigma\sqrt{1+(\Omega\tau_s/2)}\right]}{\sqrt{1+(\Omega\tau_s/2)}\cdot K_1(\sigma)}N(kl), \quad (20)$$

where $K_1(\ )$ is the modified Bessel function, and $\Omega=\omega\cdot\left(1-M_c\cos\theta\right)$. $N(kl)$ represents a non-compactness factor that is determined from the spatial function of the correlation. In Khavaran's model, the turbulent length scale and time scale are defined, respectively,

$$l_s=c_l\cdot\left(\kappa^{1.5}/\varepsilon\right)=2.943\cdot\left(\kappa^{1.5}/\varepsilon\right),\quad \tau_s=c_\tau\cdot\left(\kappa/\varepsilon\right)=0.33\cdot\left(\kappa/\varepsilon\right). \quad (21)$$

The parameter $\sigma=0.2$ is set in our calculations.

2.3 Adjoint Green Function

In general, *non-axisymmetric* jets, the adjoint-Green function can be found by solving a time-dependent, two-dimensional sound scattering problem as shown in [22]. In our current test, we are using an axisymmetric jet, for which the adjoint green function has the form:

$$\underset{r<R_0}{p^a}\left(\vec{x}_1,\vec{x},\omega\right)=\frac{-i\omega}{8\pi^2a_\infty^2R}\cdot\exp\left(i\frac{\omega}{a_\infty}\left(R-x\cdot\cos\Theta\right)\right)\sum_{m=0}^{\infty}f_m(r)\cos(m\phi), \quad (22)$$

where the function $f_m(r)$ satisfies:

$$\frac{d^2 f_m}{dr^2}+\left[\frac{-4\dfrac{\cos\Theta}{a_\infty}\cdot\dfrac{d\bar{u}}{dr}}{\left(1-\dfrac{\bar{u}\cos\Theta}{a_\infty}\right)}-\frac{1}{\bar{\rho}}\frac{d\bar{\rho}}{dr}+\frac{1}{r}\right]\cdot\frac{df_m}{dr}+\left[\frac{\omega^2\left(1-\dfrac{\bar{u}\cos\Theta}{a_\infty}\right)^2}{\left(\dfrac{\gamma\bar{p}}{\bar{\rho}}\right)}\right.$$

$$\left.+\frac{3\left(\dfrac{1}{\bar{\rho}}\dfrac{d\bar{\rho}}{dr}\cdot\dfrac{d\bar{u}}{dr}-\dfrac{1}{r}\dfrac{d\bar{u}}{dr}-\dfrac{d^2\bar{u}}{dr^2}\right)\dfrac{\cos\Theta}{a_\infty}}{\left(1-\dfrac{\bar{u}\cos\Theta}{a_\infty}\right)}-\frac{m^2}{r^2}-\frac{\omega^2\cos^2\Theta}{a_\infty^2}\right]\cdot f_m=0. \tag{23}$$

In the above equations, spherical coordinates ($R,\quad \Theta,\quad \phi$) are used for the far-field point $\vec{x}$ with the jet-axis as the polar axis; cylindrical coordinates ($r,\quad \phi,\quad x$) are used for the point $\vec{x}_1$ with the jet axis as the x-axis. The "bar" above the letters indicates the mean profile values. It is noted that for supersonic jet, Eq. (23) has a regular singular point at $r=r_c$ where $\bar{u}(r_c)\cdot\cos\Theta/a_\infty=1$. Following the approach suggested in Tam and Auriault ([23]), Eq.(26) is integrated in the complex r-plane by the Plemelj formulae ([24]).

III. Numerical Evaluation of the Adjoint Green Function

3.1 Adjoint Green Function for Subsonic Jets

In this section, numerical calculation of the adjoint Green function (AGF) is performed in a locally parallel jet flow, which is compared with the results from Kavaran et al. ([10]). The jet profiles are defined

$$\frac{\rho(r)}{\rho_\infty}=1,$$
$$\frac{U(r)}{c_\infty}=M_\infty+(M_J-M_\infty)\cdot\sec h^2(2r/D_J). \tag{24}$$

The above jet profile simulates a test situation in infinite wind tunnel (IWT) ($M_J=0.9$). Two profiles using the free-stream Mach number, $M_\infty=0.0$ (IWT0) and $M_\infty=0.18$ (IWT) have been examined. A ring source directivity factor has been calculated and compared with Khavaran's results ([25]). The ring source directivity factor is defined as

$$D^2(\vec{x},\vec{x}^s,\omega)\equiv\frac{(4\pi R)^2}{2\pi}\int_{-\pi}^{\pi}\left|p^a(\vec{x},\vec{x}^s,\omega)\right|^2 d\varphi^s.$$

Figure 1 presents the calculated ring source directivity factors at two typical locations ($r^s/D_J=0.0,\quad 0.5$) at observer Strouhal number of $St=0.50$, which compare well with Khavaran's results. Also shown in Figure 1 is the case simulating the open wind tunnel (OWT), which is defined by subtracting

$$\frac{U(r)}{c_\infty}=M_\infty\left(1-\sec h^2(2r/D_J-4)\right),\quad r>2D_J \tag{25}$$

from equation (24).

Figure 1 also demonstrates that the effect of the infinite wind tunnel, compared to the zero free-stream conditions, is a reduction of noise in the aft arc and an increase in the utmost forward arc.

3.2 Adjoint Green Function for Supersonic Jets

As pointed out by Tam and Auriault ([23]), for supersonic jet, Eq. (23) has a regular singular point at $r = r_c$ where $\bar{u}(r_c)\cdot\cos\Theta/a_\infty = 1$. For a typical jet velocity profile with $d\bar{u}/dr < 0$, Tam and Auriault suggest that Eq. (23) can be integrated over the deformed contour above the critical point as shown in Figure 2(a). In our work, Plemelj formulae is used to complete the integration, which states that for an analytical function $f(z)$, the Cauchy integral of $f(z)$, i.e., $F(z) = \frac{1}{2\pi i}\int_P \frac{f(\zeta)}{\zeta - z}d\zeta$ can be evaluated by

$$F_+(z) = \frac{1}{2}f(z) + F_P(z), \tag{26}$$

where F_P is the "Cauchy principle value" integral. Once the Plemelj formulae is applied on each term in Eq. 23 at point $r = r_c$, we obtain the following equation

$$-4\frac{d\bar{u}}{dr}\cdot\frac{df_m}{dr} + 3\left(\frac{1}{\bar{\rho}}\frac{d\bar{\rho}}{dr}\cdot\frac{d\bar{u}}{dr} - \frac{1}{r_c}\frac{d\bar{u}}{dr} - \frac{d^2\bar{u}}{dr^2}\right)\cdot f_m = 0, \tag{27}$$

Solving Eq. (30) analytically, we have

$$\frac{f_m\big|_{r_c+\delta r}}{f_m\big|_{r_c-\delta r}} = \int_{r_c-\delta r}^{r_c+\delta r} \frac{3\left(\frac{1}{\bar{\rho}}\frac{d\bar{\rho}}{dr}\cdot\frac{d\bar{u}}{dr} - \frac{1}{r_c}\frac{d\bar{u}}{dr} - \frac{d^2\bar{u}}{dr^2}\right)}{4\frac{d\bar{u}}{dr}}dr\,. \tag{28}$$

Figure 2(b) presents the calculated ring source directivity factors at a supersonic jet ($M_J = 1.6$) with the OWT profile. Compared with the subsonic jet, the zone of silence has grown in size. In Figure 2(b), the effects of the radius ($\delta r = 0.1,\ \ 10^{-2},\ \ 10^{-3}$) of the detoured integration line in the complex-r plane has also been shown, which found that at $\delta r = 10^{-3}$, the obtained AGF tends to be convergent.

IV. Far-Field Sound

Calculations of turbulence and noise in a supersonic 3D converging-diverging nozzle were carried out to assess the suitability of acoustic-analogy methods. The parameters were taken from Ref. [26]. The computational model includes both the nozzle and the plume region. The computational domain is shown in Fig. 3. The flow parameters for the C-D nozzle are shown in the Table 1 below. A six-block overset grid was generated for the convergent-divergent (CD) nozzle shown in Figure 3. The number of grid points in each block is shown in Table 2. Blocks 1 through 5 have a cylindrical topology to match the nozzle configuration. These blocks have conforming surfaces with *Ny*=16 grid points in the azimuthal direction.

Parameters	Dimensional Values	Normalized Values
Throat Diameter	5.1 (in.)	1.0
Exit Diameter	5.395 (in.)	1.058
Inlet Diameter		1.6
Distance from Throat to Exit	5.525 (in.)	1.083
Jet Exit Velocity	2409 (fps)	1.
Ambient Velocity	400 (fps)	0.166
Pressure Ratio		3.121
Stagnation Temp	1716 ($^\circ$ R)	

Table 1: Flow Parameters for the CD CD nozzle.

Block	Nx	Ny	Nz	Total No. of Points
1	41	16	41	26,896
2	41	16	81	53,136
3	11	16	81	14,256
4	41	16	41	26,896
5	41	16	81	53,136
6	20	20	57	22,800

Table 2: Number of grids points for the computational blocks around the CD nozzle.

The calculated mean velocity profiles as well as the turbulent intensities at four stream-wise locations (x/D=0.2, 1.2, 4.4, 8.7) have been shown in Figures 4 and 5, which have been compared well with the experimental results ([26]).

The aerodynamic results obtained from our CFD code (AEROFLO) were then input to our noise prediction code. For the noise prediction, there are essentially three steps carried out. First with a prescribed jet starting inflow condition, the mean flow and the values of k and ε are calculated from AEROFLO. Once k and ε are found, the turbulent time and length scales can be obtained by Equations (16) or (21). The second step is to make use of the calculated mean flow to find the adjoint Green's function as in Eq. (23). Finally, the volume integral is evaluated by dividing the jet axially into slices. It is noted that the adjoint Green's function are calculated at every angle and every radial point given an axial slice location. Figure 6 presents the ring directivity factor of the adjount Green functions at two axial locations, which are similar to the results from Figure 2.

Figure 7 present the results of the overall sound pressure level (OAPSL) from the two sound prediction methods, which have been compared with the experimental data and the results from the scaling law model in Khavaran([10]). It is noted that the predicted OASPL values are very low for small angles (less than 60^0) from Tam and Auriault's model. This character of Tam and Auriault's model was noted by Morris and Farassat ([27]). They argued that Tam and Auriault's model made distinctions on sound source mechanisms from the small-scale and large-scale turbulence. Since Tam and Auriault's model took accounts only about the fine scale turbulence noise, which are then limited to angles approximately greater than 60 deg to the jet downstream axis. The use of Khavaran's model clearly improves the OASPL prediction at the shallow angles, which however is not as good as his scaling law method. It is suspected that the sound levels at shallow angles are contaminated by some shock-associated noise, which needs further clarifications.

Figure 8 compares the sound spectrum at four angles. Once more, it demonstrates that Tam and Auriault's model performs very well at angles around 90 deg, but under predict the sound level in shallow angles. Furthermore, it is found that Tam and Auriault's model predict better at the lower frequency range than Khavaran's model.

V. Conclusion

Generally speaking, the RANS-based acoustic-analogy methods misrepresent the peak-frequency sound for small jet-axis angles. The predicted OASPL intensity is much lower than the experimental values at small jet-axis angles, especially for Tam and Auriault's model. The inaccuracy associated with this type of models, besides the empirical model constant, drive us look for a more accurate LES method to predict jet noise especially generated from large-scale turbulent structuresbetter than Khavaran's at the lower frequency range

Acknowledgments

This work is supported by Navy SBIR project #N68335-05-C-0380 with Dr. John Spyropoulos as Technical Monitor.

References

[1]Tam, C.K.W, "Supersonic Jet Noise," *Annual Reviews in Fluid Mechanics*, **27**, 17-43.

[2]Norum, T.D., et al. (2004) "Supersonic jet exhaust noise at high subsonic flight speed," NASA/TP-2004-212686.

[3]M.J. Lighthill, On sound generated aerodynamically: Part 1. General theory, *Proceedings of the Royal Society of London* A **211** (1952) 564–587.

[4]M.J. Lighthill, On sound generated aerodynamically: Part 2. Turbulence as a source of sound, *Proceedings of the Royal Society of London* A **214** (1954) 1–32.

[5]ESDU International plc, ESDU 98019 and software B9819, Computer-based estimation procedure for single-stream jet noise, 1998.

[6]M.J. Fisher, G.A. Preston, W.D. Bryce, A modelling of the noise from coaxial jets, Part 1: with unheated primary flow, *Journal of Sound and Vibration* 209 (1998) 385–403.

[7]M.J. Fisher, G.A. Preston, C.J. Mead, A modelling of the noise from coaxial jets, Part 2: with heated primary flow, *Journal of Sound and Vibration* 209 (1998) 405–417.

[8]T.F. Balsa, P.R. Gliebe, Aerodynamics and noise of coaxial jets, AIAA Journal 15 (1977) 1550–1558.

[9]R. Mani, T.F. Balsa, P.R. Gliebe, High-velocity jet noise source location and reduction, Task 2, Federal Aviation Administration Report, FAA-RD-76-II, 1978.

[10]A. Khavaran, Computation of supersonic jet mixing noise for an axisymmetric convergent-divergent nozzle, AIAA Journal of Aircraft 31 (1993) 603–612.

[11]A. Khavaran, Role of anisotropyin turbulent mixing noise, AIAA Journal 37 (1999) 832–841.

[12]A. Khavaran and J. Bridges, Modelling of fine-scale turbulence mixing noise, *Journal of Sound and Vibration* 209 (2005) 1131–1154.

[13]C.K.W. Tam, L. Auriault, Jet mixing noise from fine-scale turbulence,American Institute of Aeronautics and Astronautics Journal 37 (1999) 145–153.

[14]G.M. Lilley, The generation and radiation of supersonic jet noise, Vol. IV – theory of turbulence generated noise, noise radiation from upstream sources, and combustion noise. Part II: generation of sound in a mixing region, Air Force Aero Propulsion LaboratoryTechnical Report 72–53, 1972.

[15]Ladeinde, F., Alabi, K., Safta, C., Cai, X., Johnson, F., 2006. "The First High-order Simulation of Aircraft: Challenges and Opportunities," AIAA 2006-1526. 44th Aerospace Sciences Meeting, Reno, NV, January 2006.

[16]Safta, S., Alabi, K.. & Ladeinde, F., 2006. "Comparative Advantages of High-Order Schemes for Subsonic, Transonic and Supersonic Flows." AIAA 2006-299.

[17]Jiang, G. and Shu, C.-W., "Efficient implementation of weighted ENO schemes," *J. Comp. Phys*., **126**, pp.202, 1996.

[18]Alabi, K. and Ladeinde, F. "Parallel, high-order overset grid implementation for supersonic flows," AIAA-2004-0437.

[19]Tam, C.K.W. and Ganesan, A. (2003) "A modified k-e turbulence model for calculating the mean flow and noise of hot jets," AIAA Paper 2003-1064.

[20]Pope, S.B., "An Explanation of the Turbulent Round Jet/Plane Jet Anomaly," *AIAA J.* Vol.16(3), 1978, pp.279-281

[21]Sarkar, S. and Lakshmanan, B., "Application of a Reynolds Stress Turbulence Model to the Compressible Shear Layer, " AIAA J. Vol.29, No.5, 1991, pp.743-749.

[22]C.K.W. Tam, N.N. Pastouchenko, "Noise From Fine Scale Turbulence of Nonaxisymmetric Jets," AIAA J. 40(2), 2002, 456-464.

[23]C.K.W. Tam, L. Auriault, Mean Flow Refraction Effects on Sound Radiation from Localized Sources in a Jet, " J. Fluid Mechanics, 370(1998), 149-174.

[24]Crighton, D.G. et al. *Modern Methods in Analytical Acoustics*, Springer-Verlag Lecture Notes, p.42.

[24]Khavaran, A et al. Effect of free jet on refraction and noise, NASA/TM-2005-213821

[26]K.J. Yamamoto, *et al.* Experimental investigation of shock-cell noise reduction for single stream nozzles in simulated flight – comprehensive data report, NASA CR-168234, 1984.

[27]P.J. Morris, F. Farassat, Acoustic analogy and alternative theories for jet noise prediction, AIAA J. 40 (2002) 671–680.

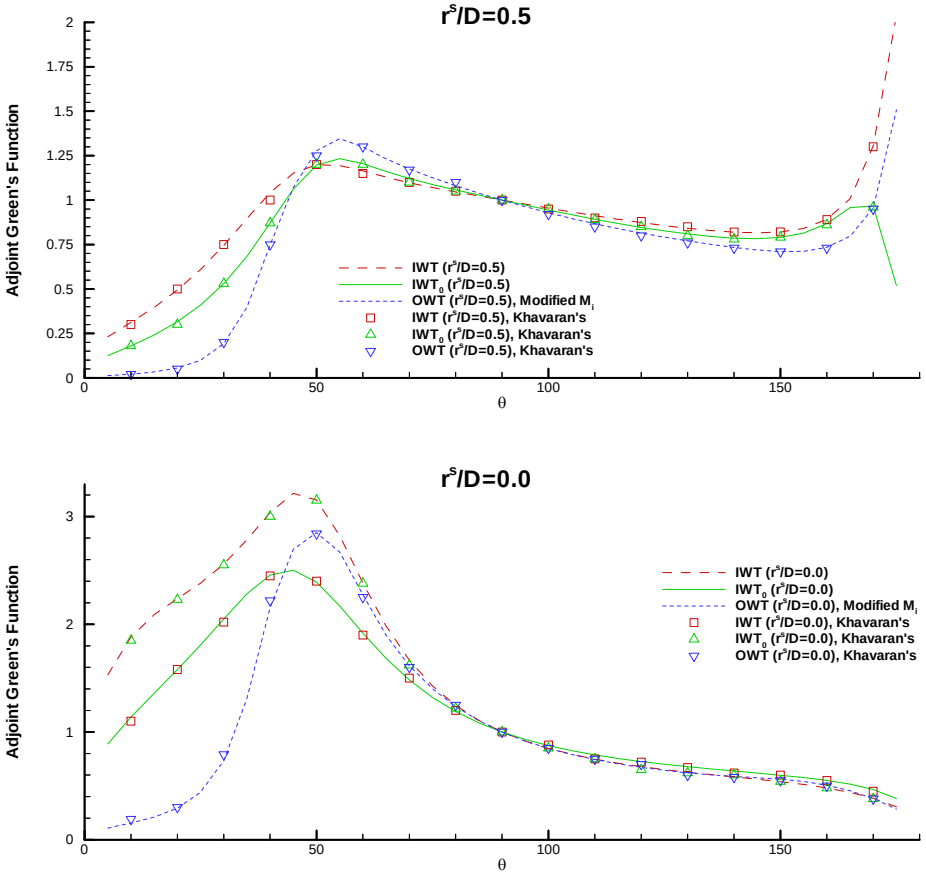

Figure 1: Ring source directivity factor of adjoinf Green functions at observer Strouhal number of $St = 0.50$ in an isothermal jet ($M_J = 0.90$).

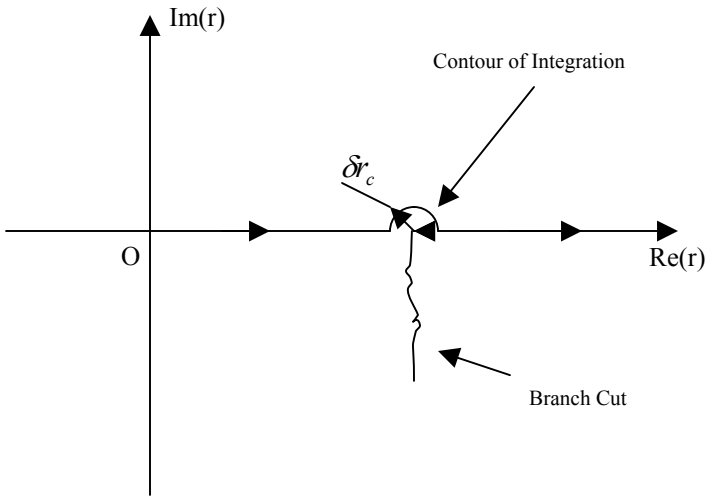

Figure 2(a): Contour of integration for calculating AGF of supersonic jets

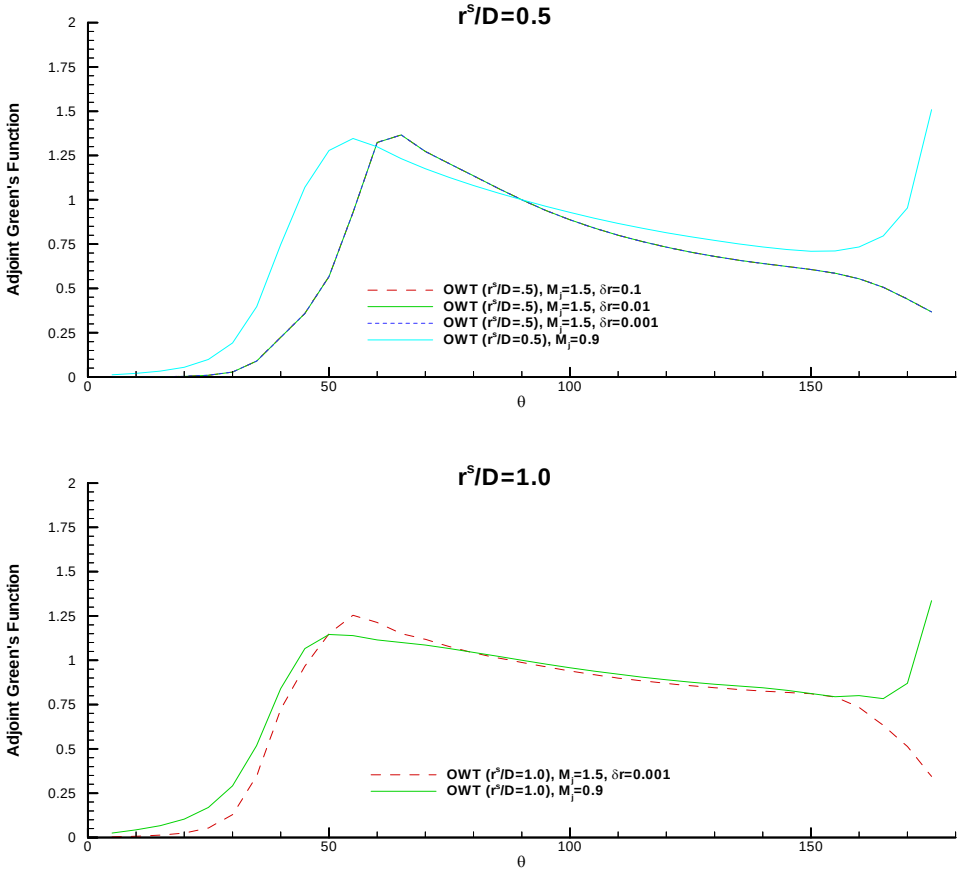

Figure 2(b): Effects of the radius of detoured integration line in Plemelj formulae on the ring source directivity factor of adjoinf Green functions at observer Strouhal number of $St = 0.50$ in an isothermal supersonic jet ($M_J = 1.60$).

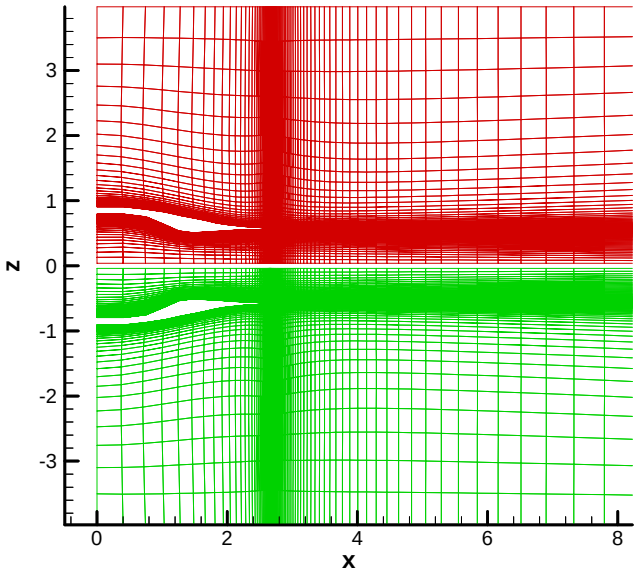

Figure 3: 2D Mesh at selected plane for CD nozzle calculations

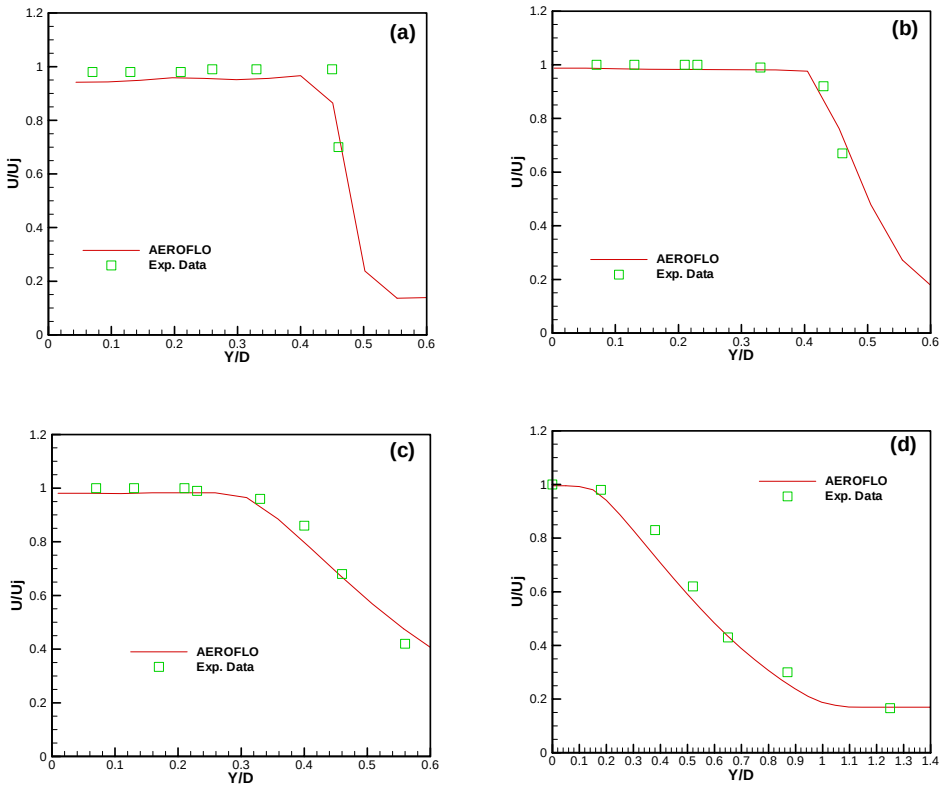

Figure 4: Comparison of the mean velocity profiles with experimental data at four axial locations: a*) x/D*=0.2; b) *x/D*=1.2; c) *x/D*=4.4; d) *x/D*=8.7

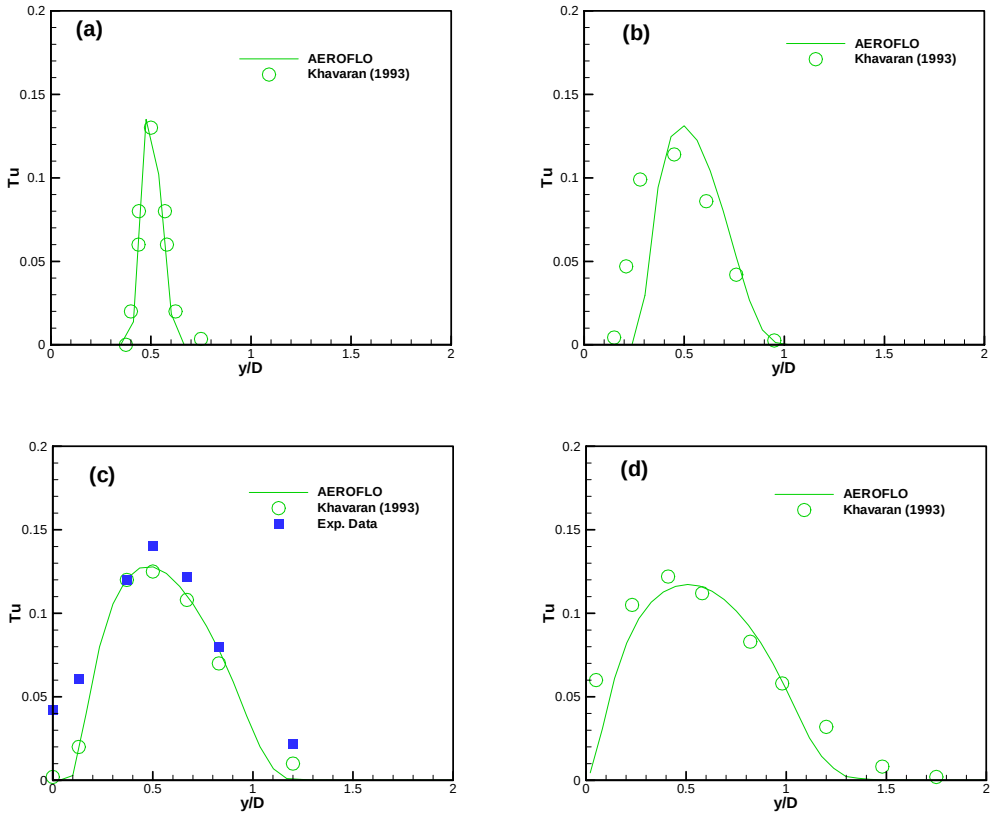

Figure 5: Comparison of the turbulent intensity profiles with experimental data at four axial locations: a*) x/D*=0.2; b) *x/D*=1.2; c) *x/D*=4.4; d) *x/D*=8.7

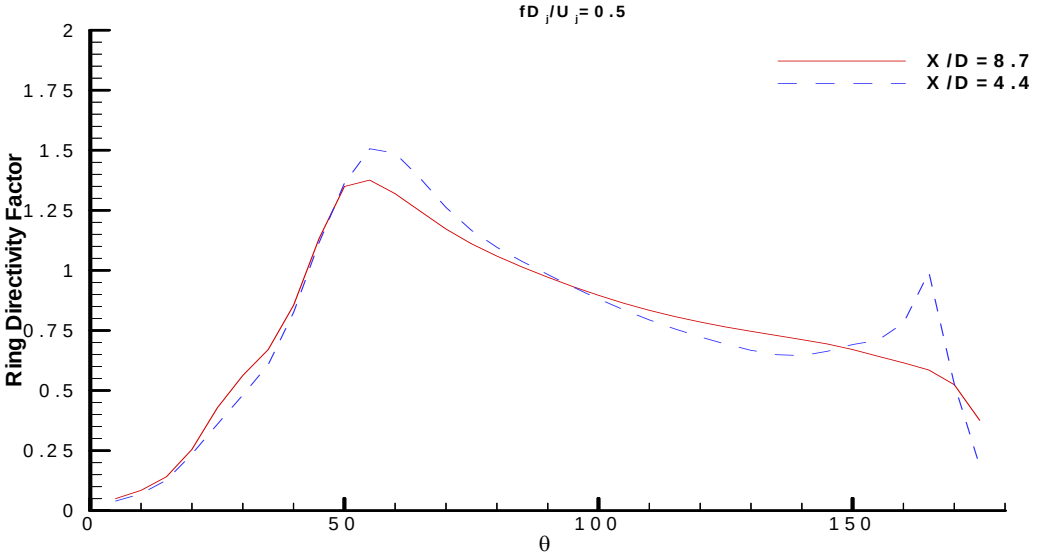

Figure 6: the ring directivity factor of the adjoint Green functions at two axial locations

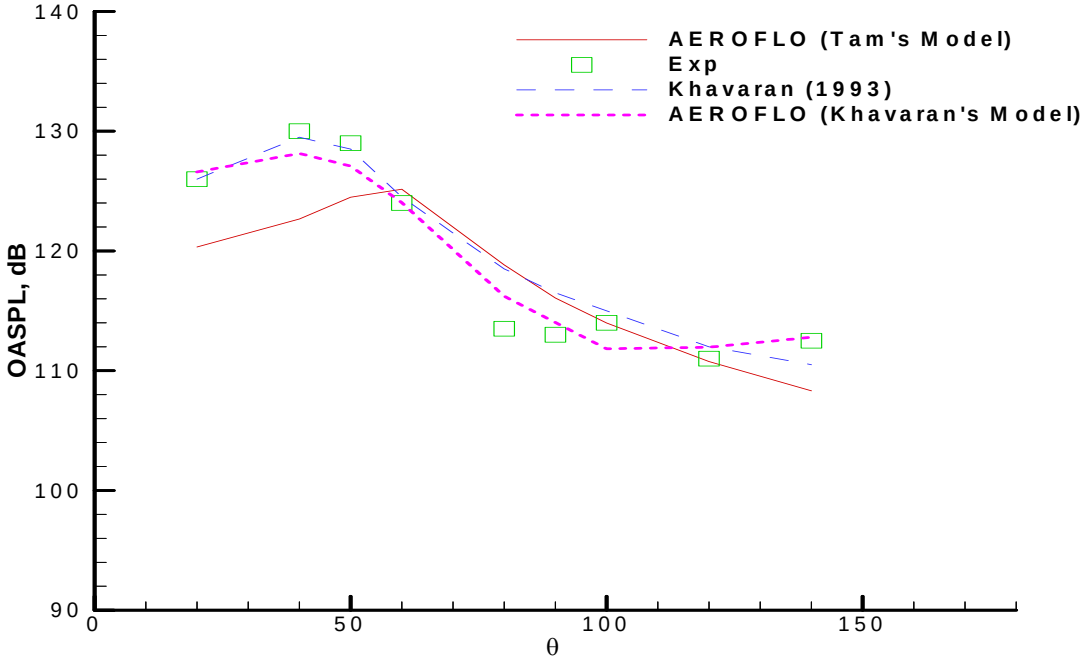

Figure 7: Comparison of the overall sound pressure level directivity

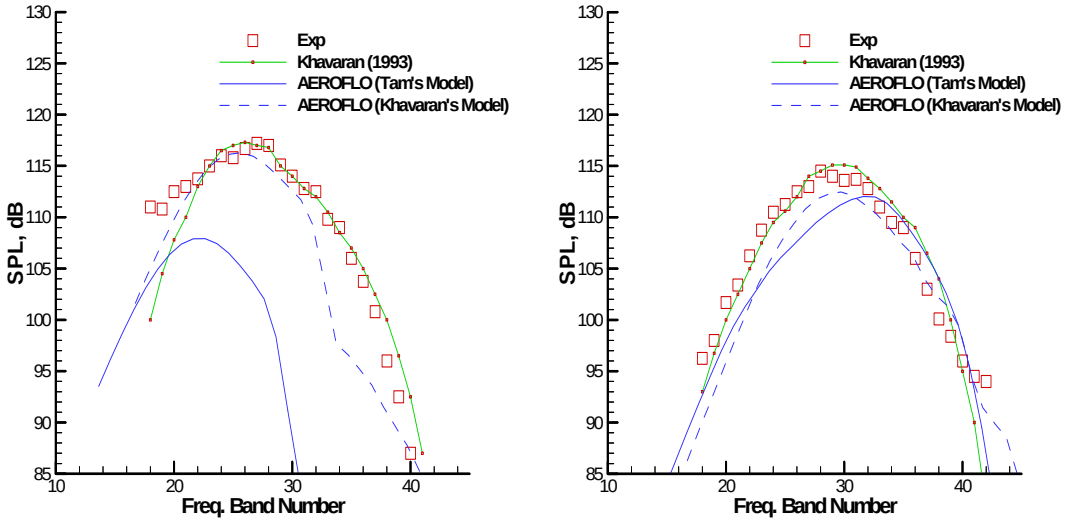

(a) (b)

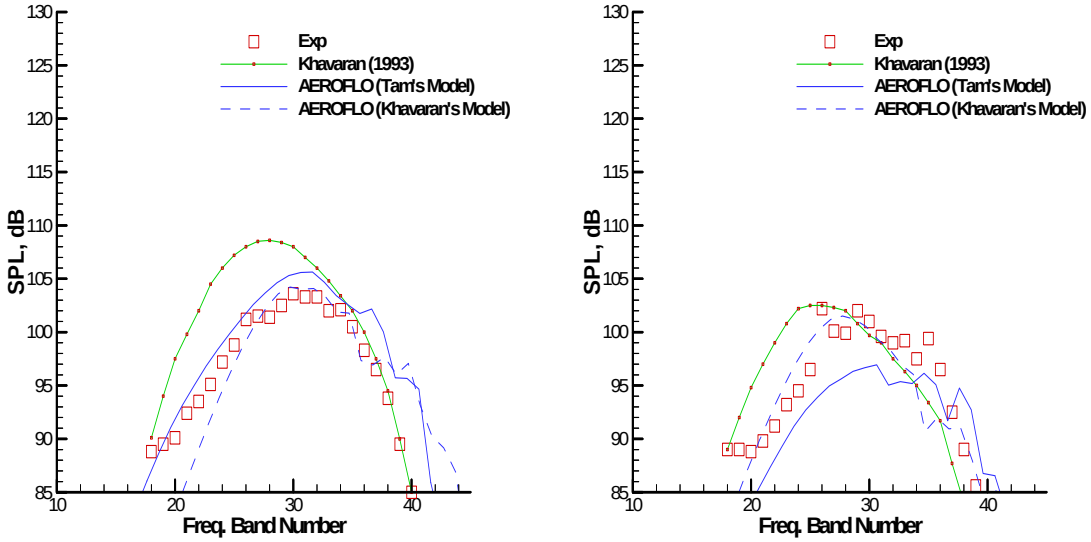

(c) (d)

Figure 8: Comparison of the sound spectrum at four angles: a) $\theta = 20^0$; b) $\theta = 60^0$; c) $\theta = 80^0$; d) $\theta = 120^0$ (The frequency band number is defined as: $n = 10 \cdot \log_{10}(f) - 6$)